

Studies of 2D Material Resistive Random-Access Memory by Kinetic Monte Carlo Simulation

Ying-Chuan Chen,^{1,2} Yu-Ting Chao,¹ Edward Chen,² Chao-Hsin Wu,^{1, a)} and Yuh-Renn Wu^{1, b)}

¹⁾*Institute of Photonics and Optoelectronics, National Taiwan University, Taipei City 10617, Taiwan*

²⁾*Corporate Research, Taiwan Semiconductor Manufacturing Co., Ltd., Hsinchu City 30078, Taiwan*

(Dated: 25 April 2023)

Resistive memory based on 2D WS₂, MoS₂, and h-BN materials has been studied, including experiments and simulations. The influences with different active layer thicknesses have been discussed, including experiments and simulations. The thickness with the best On/Off ratio is also found for the 2D RRAM. This work reveals fundamental differences between a 2D RRAM and a conventional oxide RRAM. Furthermore, from the physical parameters extracted with the KMC model, the 2D materials have a lower diffusion activation energy from the vertical direction, where a smaller bias voltage and a shorter switching time can be achieved. It was also found the diffusion activation energy from the CVD-grown sample is much lower than the mechanical exfoliated sample. The result shows MoS₂ has the fastest switching speed among three 2D materials.

I. INTRODUCTION

With the increasing popularity of artificial intelligence (AI) and the Internet of Things (IoT), the demand for storage devices is also increasing. However, traditional storage devices cannot meet such demands. For example, flash memory suffers from insufficient durability, the capacity of cache memory is too small, etc. Therefore, the demand for new types of memory has arisen accordingly. Currently, the most attention-grabbing group is called storage class memory (SCM), which is characterized by good access speed and larger cache memory capacity than before. Resistive random-access memory (RRAM) is one of them. Compared with traditional memory, RRAM has the advantages of high memory density (~ 2.5 times that of NOR FLASH), high switching speed (< 10 ns), and higher good durability ($> 10^6$ times)^{1,2}.

The commonly used materials for RRAM are mainly transitional metal oxides (TMOs), which are fabricated as a sandwich structure of metal/insulator/metal (MIM). This established the characteristic index of RRAM. Scholars began to look for the possibility of new materials. With the vigorous development of material science in recent years, two-dimensional (2D) materials have jumped into people's eyes, and some research teams have begun to use 2D materials to make RRAM, such as graphene, hexagonal boron nitride (h-BN), molybdenum disulfide (MoS₂), Tungsten disulfide (WS₂), and molybdenum ditelluride (MoTe₂)³⁻⁷. 2D materials have potential for back-end-of-line (BEOL) devices and monolithic 3-dimensional (3D) integrated circuits due to the low thermal budget⁸. WS₂ and MoS₂ are currently promising 2D candidates for logic applications attributed to their high mobility and large bandgap. To effectively suppress the delay time and the power consumption between

logic and memory layers, the embedded memory made by WS₂/MoS₂ resistive random-access memory (RRAM) can match the requirement and can be further used in the in-memory and neuromorphic computing⁹. In this work, WS₂ RRAM with different thickness have been fabricated with gold/titanium (Au/Ti) contacts. MoS₂ and h-BN 2D materials are also made for comparison. To extract the material properties, we applied Kinetic Monte Carlo (KMC) Method developed from Ginestra¹⁰ in the experimental fitting, which will help us further finding the optimized structures in the RRAM design. Unlike the analytical model, which often oversimplify the conduction mechanism, the physical based KMC Method coupled with Poisson and drift-diffusion solver can extract the diffusion activation energy and obtain the defect formation and their distribution. This can be used to estimate the thickness-dependent switching behavior. The retention failure time and the breakdown voltage predicted by the physics-based model have a good agreement with experiments. Furthermore, we find the thickness with the best On/Off ratio through the extracted WS₂ parameters and obtain temperature-dependent characteristics. Then, ion transport properties are compared for RRAM fabricated by chemical vapor deposition (CVD) and mechanical exfoliation. Finally, we compare the differences in the material properties of WS₂, MoS₂, and h-BN RRAM and discuss the feasibility of 2D RRAM.

II. METHOD

A. Device Fabrication and Measurement

This study conducted experiments and simulations on WS₂, MoS₂, and h-BN RRAM. The device structures are shown in FIG. 1 (a), (b), and (c), which use Au/Ti as the top and bottom electrodes. WS₂ is fabricated with asymmetric electrodes, and MoS₂ and h-BN are fabricated with symmetric electrodes for the experiments.

^{a)}chaohsinwu@ntu.edu.tw

^{b)}yrrwu@ntu.edu.tw

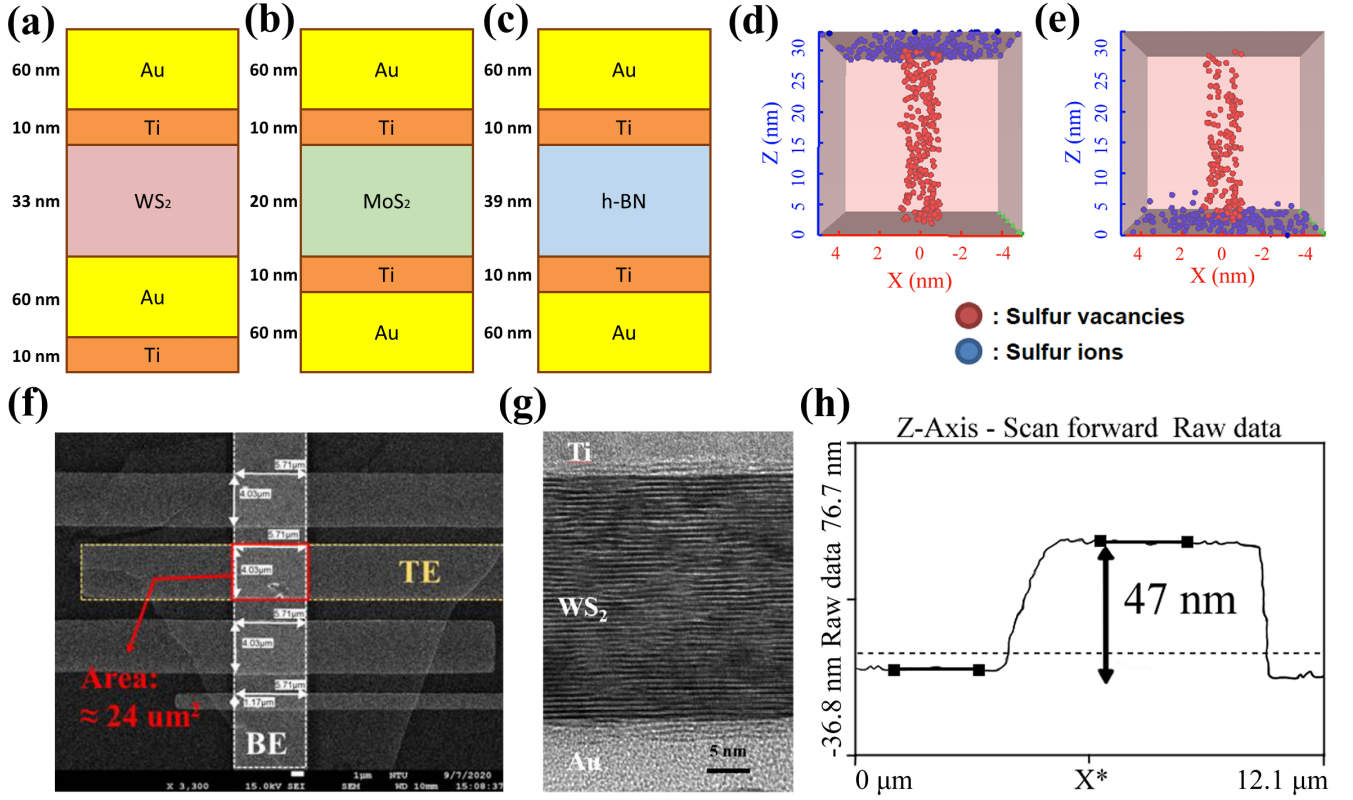


FIG. 1. (a) The schematic figures show the WS_2 , (b) MoS_2 , and (c) h-BN RRAM structures. (d) 33 nm WS_2 RRAM LRS device structure. (e) 33 nm WS_2 RRAM HRS device structure. (f) The RRAM was fabricated by exfoliated WS_2 and the conducting area was determined by the TE/BE overlap, shown in scanning electron microscopy (SEM) analysis. (g) The cross-section of the WS_2 RRAM was analyzed by TEM. (h) AFM scanning showed the WS_2 thickness.

The active layers of the devices utilized various thicknesses of WS_2 . 60 nm Au and 10 nm Ti were deposited on a heavily doped p-type silicon substrate as the bottom electrode (BE) of the RRAM device by e-gun evaporation. WS_2 flakes were obtained from single-crystal bulk material by mechanical exfoliation. Then, the flake was transferred above the BE by Polydimethylsiloxane. Afterward, Au/Ti of 60/10 nm as the top electrode (TE) was deposited on the WS_2 flake to form an asymmetric electrode WS_2 RRAM. The cross-sectional area of the RRAM device is controlled through the overlap of the TE and BE, as shown in FIG. 1 (f). The vertical structure of the device was observed and measured by transmission electron microscope (TEM) and atomic force microscope (AFM) scanning as shown in FIG. 1 (g) and (h).

B. Simulation Methodology

In this simulation, the switching state of the RRAM module was simulated to plot the I-V curve using the GinestraTM software. This software uses the kinetic Monte Carlo (KMC) Modeling^{11,12} to simulate the generation, diffusion, and recombination of defects (vacancies and ions) in the RRAM device. The physics solver

calculates the current value, including charge transport, temperature dependence, and 3D-space defects distribution. The KMC model is used to simulate the dynamic defect distribution of the active layer. The physical models of WS_2 , MoS_2 , and h-BN RRAM are built based on the experimental data, and the physical parameters of the three 2D materials are extracted.

FIG. 1 (d) and (e) are the device structures of the low resistance state (LRS) and high resistance state (HRS), respectively. It can be seen that the former has a complete conductive filament (CF), and the latter of CF becomes sparser or even fractured because ions and vacancies are recombined due to applied bias. Some defects assisting in carrier transport are recombined, causing the current to drop after the reset operation, and the trend of the current drop has a high correlation with the drift and diffusion of ions in the lattice space. In order to shorten the RRAM simulation time, we only form one CF in the small cross-sectional area model, which will cause the current drop to be discontinuous during the reset operation. Therefore, the reset I-V curve in each device is the result of averaging a lot of simulation curves. There is not only one CF formed on a large cross-sectional device, and the conduction state of each CF is different. Using the statistical averaging method can be closer to

the conduction state of the actual device.

From the distribution of ions in FIG. 1 (d) or (e), it can be seen that ions will gradually diffuse around CF so that the HRS resistance will decrease progressively with multiple resistance state switching. Therefore, the diffusion of ions in the in-plane direction is highly related to the endurance of the device. The 2D material has a polarity, which is a typical bipolar switching mode in RRAM. Usually, the forming operation is applied by a positive bias, the set operation is in the forward bias, and the reset operation is in the reverse bias. If a negative bias is applied in the forming process, the set/reset switching voltages are reversed. In the experiments, both positive and negative biases are applied in the forming operation of each device, so the set/reset bias directions may be opposite on different devices. In the simulations, a positive bias is uniformly applied for the forming operation to facilitate subsequent analysis.

The vacancies and ions are generated in the device for forming or set operation by continuously increasing applied bias. The generation rate is dependent on the 3D electric field in the device^{13,14}. This Arrhenius equation is defined as

$$R_{A,G}(x, y, z) = \nu \exp\left[-\frac{E_{A,G} - p_0(2 + \varepsilon_r)/3 \cdot F(x, y, z)}{k_B T}\right], \quad (1)$$

where ν is a frequency prefactor, $E_{A,G}$ is the zero-field generation activation energy, p_0 is the polarizability, ε_r is the relative permittivity, k_B is the Boltzmann constant, and T is the temperature. The electric field will drift Sulfur ions in the active layer. The diffusion rate depends on the local effective electric field along the diffusion direction. This Arrhenius equation is defined as

$$R_{A,D}(x, y, z) = \nu \exp\left[-\frac{E_{A,D}(x, y, z) - \gamma F_{eff}(x, y, z)}{k_B T}\right], \quad (2)$$

where $E_{A,D}$ is the diffusion activation energy, γ is the field acceleration factor, and $F_{eff}(x, y, z)$ is the local effective field along the ion diffusion direction by the unit vector $\hat{\mathbf{r}}$.

Retention time is how long a memory can retain a bit state at a specific temperature. For non-volatile memory, the most stringent requirement is the ability to retain data for more than ten years (about 3.1536×10^8 seconds) at operating temperatures up to 85°C. In order to shorten the detection time, the device will be placed in a high-temperature environment, and the changes in time and resistance value must be recorded during the baking process of the device. By changing the temperature to record the retention failure time of the device, the Arrhenius diagram can be drawn to extract the activation energy. Then it is extrapolated to the working temperature to obtain the retention time at this temperature. According to the experimental report¹⁵ by Bin Gao et al., the retention time of the device can also be calculated through generation activation energy and theoretical formulas. The generation probability of the unbiased

voltage is defined as

$$p = \exp(-E_a/k_B T), \quad (3)$$

where E_a is the generation activation energy, k_B is the Boltzmann constant, and T is the temperature. And the retention failure time of the device is defined as

$$t_E = t_0/(n|\ln(1-p)|) \approx t_0/np, \quad (4)$$

where t_0 is the oscillation period of lattice oxygen atoms, and n is the number of escape directions for ions inside the lattice (for a cube, n is substituted into 6). Usually, the probability of generation will be far less than 1, so we can take the original formula of Eq. 4 to Taylor expansion to obtain the first-order term. This can prevent the dilemma that the denominator is zero and cannot be solved.

III. RESULT AND DISCUSSION

A. Analysis of 2D RRAM Characteristics

In this work, we worked on three 2D materials, which are WS₂, MoS₂, and h-BN for comparison. More detailed studies on WS₂ materials have been made to build the accurate model for KMC simulations, which can be used for device optimizations.

FIG. 2 (a) is the measured and simulated set/reset current characteristics with 33-nm-thick WS₂ RRAM (44 layers), and the set/reset switching voltages are 0.5 and -0.6 V, respectively. The experimental data is the result of measuring 100 set/reset operation cycles, and the simulated set operation also sets a compliance current of 10^{-3} A. During the set switching, if the current is larger than 10^{-3} A, the system will terminate the simulation and record the last data point. So, the simulated current after the set operation will be slightly higher than the experimental data. The retention failure time can be calculated by substituting the atomic oscillation period and the generation activation energy extracted from our simulation to Eq. 4. Calculated from the first principle, the oscillation period of WS₂ is 18 fs¹⁶, and the retention failure time of WS₂ is 1.23×10^4 seconds at room temperature, about 3 hours. The experimental data provided by Yu-Ting Chao shows that the retention time of WS₂ can be maintained to 10^4 seconds. The experimental results of other researchers also show that the retention time of WS₂ can reach 10^4 seconds^{17,18}.

FIG. 2 (b) is the measured and simulated set/reset I-V characteristics of 20-nm-thick MoS₂ RRAM. The switching voltages are 0.9 and -0.9 V, and the current of reset switching dropping trend is rapider than that of WS₂. It means that the field acceleration factor of MoS₂ is higher. The generation activation energy of MoS₂ extracted is 1.13 eV, the oscillation period is 21.51 fs³², and the retention failure time at room temperature is estimated to be 3.18×10^4 seconds, about 8 hours. The experimental

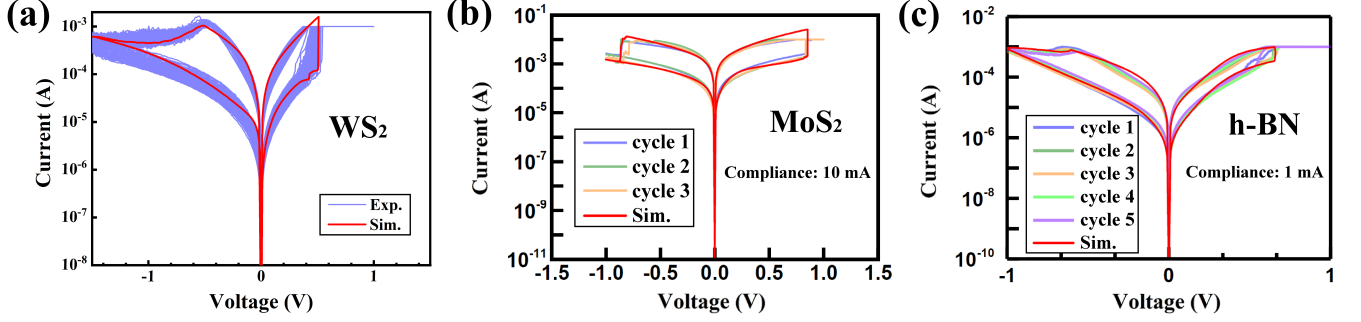


FIG. 2. (a) 33 nm WS₂ RRAM set/reset I-V characteristics. (b) 20 nm MoS₂ RRAM set/reset I-V characteristics¹⁹. (c) 39.4 nm h-BN RRAM set/reset I-V characteristics¹⁹.

TABLE I. Basic parameters of WS₂, MoS₂ and h-BN.

Parameter	Description	WS ₂	MoS ₂	h-BN
ϵ_r	Relative permittivity	6 ²⁰	7.1 ²¹	5.65 ²²
E_g (eV)	Bandgap	1.54 ²⁰	1.23 ²³	5.97 ²⁴
E_a (eV)	Electron affinity	3.92 ²⁰	4.2 ²⁵	0.8 ²⁴
k_{th} (W · cm ⁻¹ · K ⁻¹)	Thermal conductivity	1.21 ²⁶	0.035 ²⁷	7.51 ²⁸
m_e (m ₀)	Electron density of states effective mass	0.631 ²⁹	0.73 ³⁰	0.93 ³¹
m_h (m ₀)	Hole density of states effective mass	0.832 ²⁹	0.78 ³⁰	0.77 ³¹

results of other researchers also show that the retention time of MoS₂ can reach 10⁴ seconds³³.

FIG. 2 (c) is the measured and simulated set/reset I-V characteristics of 39.4-nm-thick h-BN RRAM. The switching voltages are 0.65 and -0.6 V, and the current of reset switching dropping trend is smoother than that of WS₂. It means that the field acceleration factor of h-BN is lower. The generation activation energy of h-BN extracted is 1.28 eV, the oscillation period is 24.4 fs³⁴, and the retention failure time at room temperature is estimated to be 1.18×10^7 seconds, about 136 days. The experimental results of other scholars also show that the retention time of h-BN can reach 10⁷ seconds³⁵. Although h-BN has a larger bandgap, the contact between h-BN and Ti will cause the Fermi level of the electrode to be fixed on the p-type bandgap²⁴. The defects are generated in the depth of the bandgap due to the distribution of the Fermi level, and these vacancies can only transport a tiny current. Therefore, the difference between HRS and LRS current is still tiny, and the On/Off ratio of h-BN cannot get great improvement.

TABLE I sorts out the basic parameters used by three kinds of 2D materials in this simulation. TABLE II sorts out the simulation parameters used by the three 2D materials and another hafnium oxide (HfO_x) RRAM research³⁶. WS₂ and MoS₂ have similar generation activation energy, and their retention failure times are in the same order. The diffusion activation energy of MoS₂ in the out-of-plane direction is lower than that of WS₂, and the field acceleration factor is higher. It means that sulfur ions are easier to drift and transport inside MoS₂. The reason is speculated to be related to the mass den-

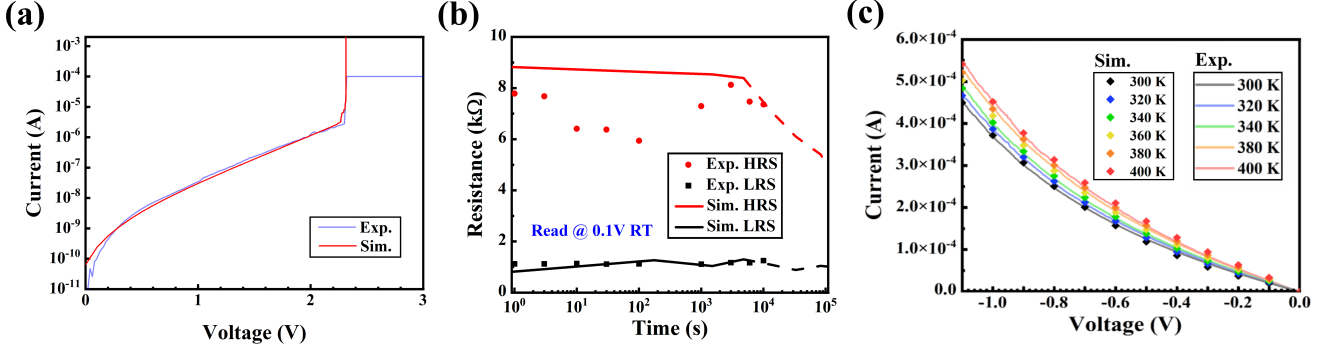
sity of the material. The mass density of MoS₂ is 5.06 g/cm³³⁷, and WS₂ is 7.5 g/cm³³⁸. This makes the drift resistance of sulfur ions inside MoS₂ less by the collision between atoms, so the transport speed is faster. The reset switching current drops more rapidly.

The generation activation energy of h-BN is the highest among the three 2D materials and has a long retention failure time. Its field acceleration factor is much lower than WS₂ and MoS₂, so the decrease of reset switching is very small. This parameter characteristic can explain why h-BN produces the phenomenon of threshold switching¹⁹ in the experiment. Therefore, h-BN needs to be applied with enough large operating power to completely separate ions and vacancies, forming non-volatile memory with stable CFs. Otherwise, ions and vacancies can only be stretched outward, forming electric dipoles. After removing the applied electric field, ions will recombine with vacancies, exhibiting the characteristics of volatile memory.

Because HfO_x RRAM has higher activation energy, the retention failure time at room temperature can exceed ten years. So, HfO_x had been widely studied in RRAM applications. The On/Off ratio of the WS₂ RRAM is about 10 at 0.1 V, and that of the HfO_x RRAM is about 50³⁶. The On/Off ratio of WS₂ RRAM is five times smaller because the bandgap of WS₂ is smaller than that of HfO_x. This makes the background current (is not the current transported through the defect) of WS₂ is relatively larger, resulting in a smaller difference between the resistance of HRS and LRS. It causes the On/Off ratio of the overall device to be rather poor. Therefore, choosing a material with a large bandgap to make an RRAM

TABLE II. Simulation parameters and switching time of WS_2 , MoS_2 , h-BN, and HfO_x ³⁶ RRAM.

Parameter	Description	WS_2	MoS_2	h-BN	HfO_x ³⁶
$E_{A,G}$ (eV)	Generation activation energy	1.11	1.13	1.28	2.9
$E_{A,D}(X/Y)$ (eV)	Diffusion activation energy of ion in X/Y direction	0.7	0.7	0.7	0.7
$E_{A,D}(Z)$ (eV)	Diffusion activation energy of ion in Z direction	0.39	0.2	0.38	0.7
E_T (eV)	Thermal ionization energy of vacancy	0.4 ± 0.04	0.3 ± 0.04	3.3 ± 0.05	—
ν (Hz)	Frequency prefactor	4.5×10^{13}	4.5×10^{13}	4.5×10^{13}	7×10^{13}
p_0 (eÅ)	Polarizability	9	29	75	5.2
γ (eÅ)	Field acceleration factor	0.2	0.4	0.01	0.2
t_R (sec)	Retention failure time	1.23×10^4	3.18×10^4	1.18×10^7	—
t_S (sec)	Switching time	3×10^{-4}	5×10^{-6}	7×10^{-5}	—

FIG. 3. (a) 12 nm WS_2 RRAM forming I-V characteristics¹⁹. (b) WS_2 RRAM retention characteristics. The dotted line is simulated prediction. (c) WS_2 RRAM HRS temperature-dependent I-V characteristics.

device can usually obtain a higher On/Off ratio.

Compared with the benchmark device (HfO_x RRAM³⁶), Our research shows that 2D RRAM has a lower generation activation energy to generate defects at a smaller bias. The diffusion activation energy of ions along the in-plane direction (i.e., X-Y plane) is greater than that of the out-of-plane direction (i.e., Z direction), which means that ions tend to diffuse along the out-of-plane direction. The reason may be due to the polar molecules between the layers. It is caused by the electrostatic attraction (van der Waals force) along the out-of-plane direction and the electromagnetic repulsion force along the in-plane direction of adjacent atoms in the same layer. Under the 2D layered molecular arrangement, the torque perpendicular to the plane is more likely to cause molecular bond breaking to form the defects, which act as channels for the transport of ions. Therefore, the set/reset switching voltage of 2D RRAM is lower than that of HfO_x , which means 2D RRAM has a faster resistance switching speed. It can be seen from the data in TABLE II that MoS_2 has the shortest switching time. So, MoS_2 is the most suitable for making RRAM devices among the three 2D materials.

In order to verify the reliability of the KMC model, we will conduct a series of experiments and simulation comparisons for WS_2 in the next section.

B. Comparison of WS_2 RRAM experiments and simulations

1. Forming Operation

FIG. 3 (a) is the measured and simulated forming current characteristics of the RRAM device made of a 12-nm-thick WS_2 (16 layers) flake. We can see that the device begins to break down at 2.3 V, and the defects inside the material start to generate in large quantities, causing the current to rise rapidly. In the experiment, a compliance current will be set to prevent the over-reaction of the material from causing the device to burn, so the current will be limited to 10^{-4} A when the applied voltage is larger than 2.3 V. The simulation can calculate the current characteristics of the device that has not been burned so the current continues to rise. After performing the forming operation, we will output the device model on the compliance current to keep going the simulation of reset and set.

2. Retention Time

FIG. 3 (b) is the measured and simulated data at a reading voltage of 0.1 V. The solid dots are the HRS and LRS resistances measured in the experiment, which only recorded to 10^4 seconds. It shows that the retention time

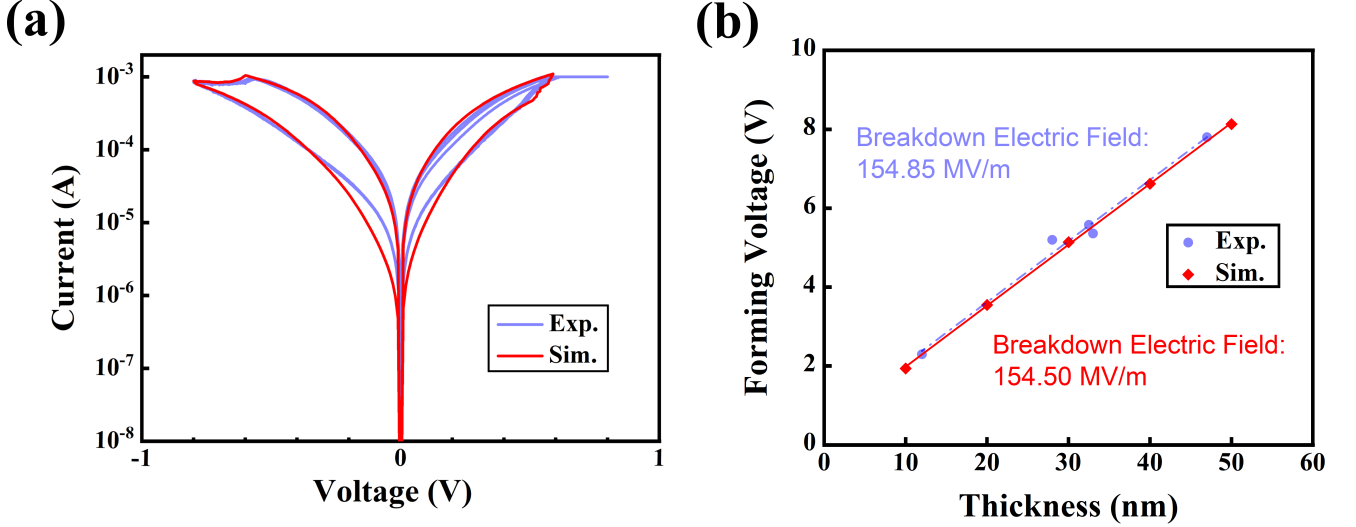


FIG. 4. (a) CVD WS₂ RRAM set/reset I-V characteristics. (b) Correlation between thickness and breakdown voltage of WS₂ RRAM.

of WS₂ can be maintained at least to 10⁴ seconds. The solid line is the resistance calculated in this simulation, and the actual device will reduce the HRS resistance due to switching multiple times. Therefore, it is reasonable that the simulated On/Off ratio is slightly larger than the experimental result. The dotted line is the result of the simulated prediction. It can be observed in FIG. 3 (b) that the HRS resistance drops sharply after 10⁴ seconds. The resistance state cannot maintain stably. This result is in good agreement with the previous the retention failure time (1.23×10^4 seconds) calculated by Eq. 4. It can be speculated that the resistance of the HRS experimental data falling to 6 k Ω has a high probability due to experimental measurement error. The LRS experiment and simulation data all show a stable resistance state at 1 k Ω .

3. Temperature-Dependent Analysis

24-nm-thick WS₂ (32 layers) was measured electrical characteristics in the temperature-dependent experiment, and the state of this device was HRS. The specific heat density and thermal conductivity used to simulate heat conduction are $1.19 \text{ J} \cdot \text{cm}^{-3} \cdot \text{K}^{-1}$ and $1.21 \text{ W} \cdot \text{cm}^{-1} \cdot \text{K}^{-1}$ ²⁶. The simulation and the experimental data are in good agreement, and the 360 K data missing from the experiment was added to FIG. 3 (a) by simulation. From the experimental trend of the adjacent temperature (340 and 380 K), it can be reasonably judged that there is no problem with the corrected data. In the ambient temperature range from 300 to 400 K, when the temperature rises, the current also rises proportionally. when the applied bias increases, the current difference of adjacent temperature will also increase. this mean the temperature-dependent characteristics will significantly

affect the current. Therefore, we must take into account the change of the ambient temperature on the current when WS₂ RRAM works at high bias.

4. CVD-Grown WS₂ RRAM Analysis

In this section, we study the differences in electrical characteristics and material properties of WS₂ RRAM fabricated by mechanical exfoliation and CVD. The previous WS₂ RRAM used mechanical exfoliation to obtain 2D flakes. In this experiment, the device used CVD technology to grow WS₂ flakes, which are ultra-thin devices with a thickness of 3 nm (4 layers). Therefore, it is necessary to fine-tune some parameters in this simulation. We change the basic parameters of the WS₂ bulk material to that of the three or four layers. For example, the bandgap was increased from the original 1.54 eV to 2.76 eV³⁹ to simulate the carrier properties of the low-number-layer semiconductor device. The experimental and simulated results are shown in FIG. 4 (a). The ultra-thin thickness makes the tunneling effect gradually obvious so that the overall current rises greatly with the applied bias.

TABLE III sorts out the simulation parameters used in mechanical exfoliation and CVD WS₂ RRAM. The generation activation energy, polarizability, and frequency prefactor of the two are the same. It indicates that the generation of defects has nothing to do with the arrangement state between layered molecules. It has a high correlation with the bond breaking of material molecular and induced electric field between polar molecules. The most obvious difference between the two fabricated methods lies in the drift and diffusion of sulfur ions inside the device. The WS₂ samples obtained by mechanical exfoliation mostly belong to the single crystal structure, and the WS₂ grown by CVD mostly belong to the poly-

TABLE III. Simulation parameters and switching time of WS₂ RRAM with mechanical exfoliation and CVD.

Parameter	Mechanical Exfoliation	CVD
$E_{A,G}$ (eV)	1.11	1.11
$E_{A,D}(X/Y)$ (eV)	0.7	0.7
$E_{A,D}(Z)$ (eV)	0.39	0.36
E_T (eV)	0.4 ± 0.04	0.75 ± 0.04
ν (Hz)	4.5×10^{13}	4.5×10^{13}
p_0 (eÅ)	9	9
γ (eÅ)	0.2	0.4
t_R (sec)	1.23×10^4	1.23×10^4
t_{switch} (sec)	3×10^{-4}	9×10^{-5}

crystalline structure. Therefore, CVD WS₂ has smaller domains and more defects. It means that each layer has more gaps and vacancies, and the probability of sulfur ion drifting and diffusing between the upper and lower layers is greatly increased.

Comparing with the simulation results of the two can be seen that the CVD WS₂ RRAM has a lower out-of-plane diffusion activation energy and a higher field acceleration factor, so it has a faster reset switching speed and a lower switching voltage. Moreover, the CVD WS₂ device has many defects. It makes the required voltage for the forming operation is lower, and the switching time is shorter. In other words, the switching power consumption is lower. The experiment also confirmed this result. Therefore, WS₂ obtained by CVD is more suitable for making RRAM devices than mechanical exfoliation.

5. Breakdown Electric Field

The experiment measured the breakdown voltage of five devices with different thicknesses, and the thicknesses of 10, 20, 30, 40, and 50 nm were used for RRAM modeling in the simulation. We assume that the device is an ideal defect-free material at the beginning, and WS₂ parameters of TABLE II were used to simulate. The simulated results are consistent with the experimental data, as shown in FIG. 4 (b). The breakdown electric field can be extracted through the thickness of WS₂ and the breakdown voltage. The experimental and simulated results show that the breakdown electric field of WS₂ is 155 MV/m. When the internal electric field is larger than 155 MV/m, defects will generate in the device. It causes the current to rise rapidly, and the initial forming operation will be performed. We also tried to use the initial model of a few defects to simulate the forming operation of natural materials. The result shows that the internal electric field generated by adding a few defects is not enough to affect the breakdown voltage. The breakdown voltage is the same as that of an ideal defect-free model.

C. Simulated Prediction

Following the previous section, the simulation is carried out with the extracted WS₂ parameters to find which thickness with the best On/Off ratio. The simulated result can get a stable I-V characteristic curve as shown in FIG. 5 (a). The stopping voltage and compliance current of each thickness are set to -1.5 V and 10^{-3} A. From the TE and BE bias and the vertical electric field formula ($F = V/d$), it can be known the thinner device has a smaller switching voltage. This inference is consistent with our simulation results. It can also be observed the current of the thinner device drops more rapidly during reset switching. The vertical electric field of the thicker device increasing value is smaller by the sweeping bias, and the drift distance of ions in the vertical direction inside the device is longer. They make overall ion drift speed slower and switching time longer. Therefore, the current declining curve is more smooth. After all the ions drift from the TE to the BE, there are not any ions and vacancies to occur bonding recombination reaction. The current of the element will gradually increase with the increase of the bias voltage at this moment.

From the current trend of each thickness in FIG. 5 (a), we can know the current of the thicker device can drop to a lower value during the reset operation because the total number of defects inside the thicker device is more. It makes the difference in the defect number larger between HRS and LRS, and the current difference is also more. For the thickness reaching 40 nm or thicker, the ions diffusing in the in-plane direction and the vertical distance increasing make the difference of the defect number gradually become less. So, the HRS current tends to be the same level. The On/Off ratio difference is small. TABLE IV sorts out the current and On/Off ratio of each thickness at -0.1 and 0.1 V reading bias. It can be found that a 40-nm-thick device has the best On/Off ratio, which can avoid bit reading errors as much as possible. Thinner devices have a faster switching speed and less energy consumption, but their On/Off ratios are relatively small. This also explains that low-layer-number 2D materials are hardly made into RRAM devices.

TABLE IV. On/Off ratio of WS₂ RRAM at ± 0.1 V for various thicknesses.

Thickness (nm)	On/Off Ratio at -0.1 V	On/Off Ratio at 0.1 V
10	5.56	3.20
20	6.14	7.89
30	7.05	14.43
40	10.13	17.43
50	6.38	17.10

Since MoS₂ has the fastest switching speed among the three 2D materials, we also conduct electrical simulations for MoS₂ RRAM at various thicknesses. The simulated method is the same as that in the previous section. The

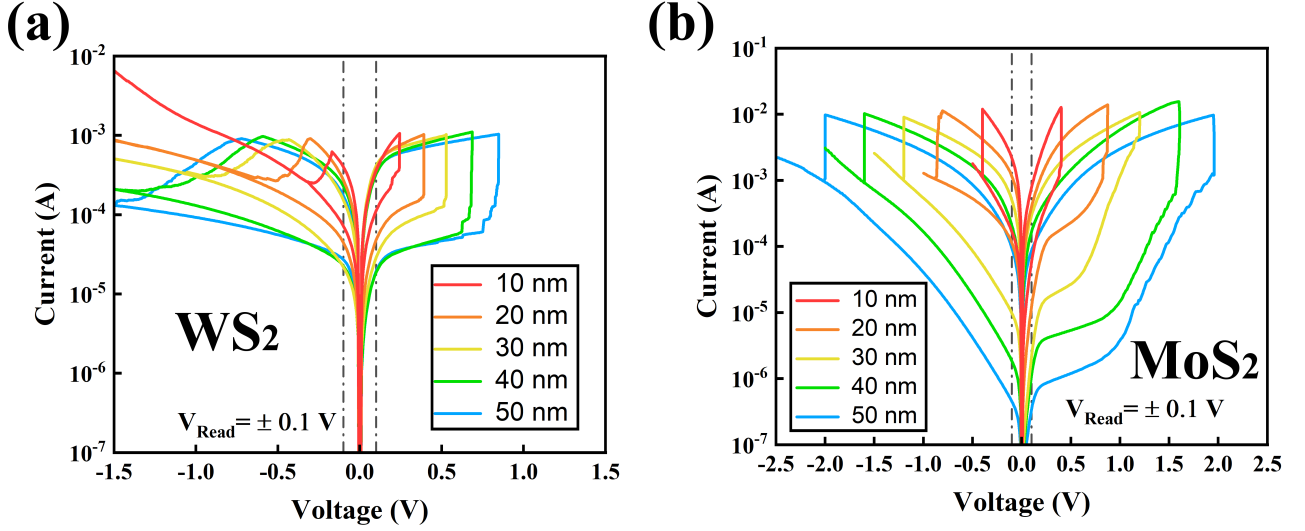


FIG. 5. (a) WS₂ RRAM set/reset I-V characteristics of various thicknesses. (b) MoS₂ RRAM set/reset I-V characteristics of various thicknesses.

TABLE V. On/Off ratio of MoS₂ RRAM at ± 0.1 V for various thicknesses.

Thickness (nm)	On/Off Ratio at -0.1 V	On/Off Ratio at 0.1 V	Stopping Voltage (V)
10	12.98	13.47	-0.4
20	18.73	32.66	-0.86
30	51.39	137.54	-1.2
40	111.94	149.16	-1.6
50	208.68	253.84	-2.0

difference is the stopping voltage is set according to the state of the reset operation of each thickness. The stopping voltages of 10 to 50 nm are -0.5, -1.0, -1.5, -2.0, and -2.5 V so that the devices can be fully reset to get the maximum on/off ratio.

From FIG. 5 (b), it can be confirmed that the thicker device has a larger On/Off ratio. The On/Off ratio of each thickness is sorted into TABLE V. It can be known that the 50 nm MoS₂ RRAM has the largest switching ratio. The value is higher than 200, which is much larger than that of WS₂ RRAM. Therefore, MoS₂ is more suitable for making an RRAM device than WS₂ in terms of switching speed and On/Off ratio.

It can be known from TABLE V that the thicker device has a greater switching voltage, which will lead to greater power consumption. The stopping voltage of 50 nm devices must be set to a reverse bias voltage greater than 2.0 V. The thickness of RRAM should be determined according to the given operating voltage (V_{DD}) and power consumption constraints on the overall circuit system, and the current noise should be reduced to less than the device On/Off ratio to avoid memory misinterpretation.

IV. SUMMARY

We built physical models of WS₂, MoS₂, and h-BN RRAM through KMC simulation and experimental data and extracted the physical parameters of the three 2D materials. Through theoretical formulas, we also calculated the retention failure times of WS₂, MoS₂, and h-BN RRAM, which are respectively 1.23×10^4 , 3.18×10^4 , and 1.18×10^7 seconds. Compared with the HfO_x RRAM (benchmark device), the models show the ions prefer to drift in the out-of-plane direction due to the molecular arrangement structure of the 2D material. It results in the 2D RRAM having a lower threshold voltage, which makes the device switching time faster. In particular, the switching speed of MoS₂ RRAM is the fastest in three 2D RRAM. To verify the reliability of the KMC model, we conducted a comparative analysis of the temperature-dependent experiment and the simulation for WS₂ RRAM. The results showed that the current characteristics at high bias voltage are more significantly affected by the temperature change. We discussed the physical characteristics of RRAM made of 2D materials obtained by mechanical exfoliation and CVD technology. The results show that 2D materials grown by CVD have better device characteristics and are more suitable for making RRAM. Finally, electrical analysis and simulation for different active layer thicknesses were conducted to obtain the breakdown electric field of WS₂ as 155 MV/m, and built the thickness models to simulate the On/Off ratio and switching voltage of WS₂ and MoS₂ RRAM at various thicknesses for reference in future 2D RRAM device design.

If high-retention RRAM devices are wanted to make, we suggest that the active layer can choose materials with high generation activation energy (i.e., bond-dissociation

energy) to improve retention. Although h-BN has a high retention failure time, its current difference is too low due to low electron affinity. When h-BN is in contact with the metal, the Fermi level will be pinned on the p-type. It results that h-BN RRAM can only generate deep-level defects to make a low On/Off ratio. Therefore, h-BN is not an ideal RRAM material. The RRAM materials with better retention should be outside the scope of 2D materials due to the conditions of high bandgap, high electron affinity, and high bond-dissociation energy. For the development of 2D RRAM, the rapid drift of ions in 2D materials helps to manufacture RRAM devices with faster switching speeds. This advantage can solve the slow switching speed of traditional solid-state disks and the volatile memory property of DRAM. 2D RRAM can make up for the speed gap of the memory hierarchy⁴⁰. To find the faster switching speed RRAM, 2D RRAM can carry out more in-depth experimental and simulated studies on MoS₂ RRAM in the future.

ACKNOWLEDGMENTS

Yu-Ting Chao fabricated and measured the devices for WS₂. Tzu-Heng Wang fabricated and measured the devices for MoS₂ and h-BN. Ying-Chuan Chen simulated various devices and analyzed data. Ying-Chuan Chen wrote the manuscript. All the authors discussed the results and explanations.

This work was supported by the National Science and Technology Council under Grant Nos. NSTC 111-2221-E-002-075, 111-2622-8-002-001, 112-2119-M-002-013 and 111-2218-E-002-025.

REFERENCES

- ¹S. Yu and P.-Y. Chen, "Emerging memory technologies: Recent trends and prospects," *IEEE J. Solid-State Circuits* **8**, 43–56 (2016).
- ²M.-T. Li, "Development and challenges of the new non-volatile memory," *Nano Commun. Netw.* **21**, 9–14 (2014).
- ³R. Singh, R. Kumar, A. Kumar, D. Kumar, and M. Kumar, "Enhanced resistive switching in graphene oxide based composite thin film for nonvolatile memory applications," *MRX* **6**, 105621 (2019).
- ⁴X. Hou, R. Pan, Q. Yu, K. Zhang, G. Huang, Y. Mei, D. W. Zhang, and P. Zhou, "Tubular 3d resistive random access memory based on rolled-up h-bn tube," *Small* **15**, 1803876 (2019).
- ⁵X.-F. Wang, H. Tian, H.-M. Zhao, T.-Y. Zhang, W.-Q. Mao, Y.-C. Qiao, Y. Pang, Y.-X. Li, Y. Yang, and T.-L. Ren, "Interface engineering with MoS₂ – pd nanoparticles hybrid structure for a low voltage resistive switching memory," *Small* **14**, 1702525 (2018).
- ⁶Y. Li, M. Sivan, J. X. Niu, H. Veluri, E. Zamburg, J. Leong, U. Chand, S. Samanta, X. Wang, X. Feng, *et al.*, "Aerosol jet printed WSe₂ based RRAM on kapton suitable for flexible monolithic memory integration," in *2019 IEEE International Conference on Flexible and Printable Sensors and Systems (FLEPS)* (IEEE, 2019) pp. 1–3.
- ⁷F. Zhang, H. Zhang, P. Shrestha, Y. Zhu, K. Maize, S. Krylyuk, A. Shakouri, J. Campbell, K. Cheung, L. Bendersky, A. V. Davydov, and J. Appenzeller, "An ultra-fast multi-level MoTe₂-based RRAM," in *2018 IEEE International Electron Devices Meeting (IEDM)* (2018) pp. 22.7.1–22.7.4.
- ⁸A. Bablich, S. Kataria, V. Passi, and M. C. Lemme, "Graphene and two-dimensional materials: Extending silicon technology for the future?" in *Integrated Nanodevice and Nanosystem Fabrication* (Jenny Stanford Publishing, 2017) pp. 27–74.
- ⁹M. D. Bishop, H.-S. P. Wong, S. Mitra, and M. M. Shulaker, "Monolithic 3-d integration," *IEEE Micro* **39**, 16–27 (2019).
- ¹⁰A. Padovani, L. Larcher, O. Pirrotta, L. Vandelli, and G. Bersuker, "Microscopic modeling of HfO_x RRAM operations: From forming to switching," *IEEE T-ED* **62**, 1998–2006 (2015).
- ¹¹A. F. Voter, "Introduction to the kinetic monte carlo method," in *Radiation effects in solids* (Springer, 2007) pp. 1–23.
- ¹²D. T. Gillespie, "A general method for numerically simulating the stochastic time evolution of coupled chemical reactions," *J. Comput. Phys.* **22**, 403–434 (1976).
- ¹³J. McPherson, J. Kim, A. Shanware, and H. Mogul, "Thermochemical description of dielectric breakdown in high dielectric constant materials," *Appl. Phys. Lett.* **82**, 2121–2123 (2003).
- ¹⁴A. Padovani, D. Gao, A. Shluger, and L. Larcher, "A microscopic mechanism of dielectric breakdown in SiO₂ films: An insight from multi-scale modeling," *Journal of Applied physics* **121**, 155101 (2017).
- ¹⁵B. Gao, J. Kang, H. Zhang, B. Sun, B. Chen, L. Liu, X. Liu, R. Han, Y. Wang, Z. Fang, *et al.*, "Oxide-based RRAM: Physical based retention projection," in *2010 Proceedings of the European Solid State Device Research Conference* (IEEE, 2010) pp. 392–395.
- ¹⁶T. H. Ho, V. Q. Bui, T. B. Phan, Y. Kawazoe, and H. M. Le, "Atomistic observation of the collision and migration of Li on MoSe₂ and WS₂ surfaces through ab initio molecular dynamics," *PCCP* **19**, 27332–27342 (2017).
- ¹⁷H. An, Y. H. Lee, J. H. Lee, C. Wu, B. M. Koo, and T. W. Kim, "Highly stable and flexible memristive devices based on polyvinylpyrrolidone: WS₂ quantum dots," *Sci. Rep.* **10**, 1–8 (2020).
- ¹⁸J. H. Lee, C. Wu, S. Sung, H. An, and T. W. Kim, "Highly flexible and stable resistive switching devices based on WS₂ nanosheets: poly (methylmethacrylate) nanocomposites," *Sci. Rep.* **9**, 1–8 (2019).
- ¹⁹T.-H. Wang and C.-H. Wu, *The research of 2D material-based Resistive Random Access Memory and 1T-1R cell*, Master's thesis, National Taiwan University (2020).
- ²⁰S. Roy and P. Bermel, "Electronic and optical properties of ultra-thin 2d tungsten disulfide for photovoltaic applications," *Sol. Energy Mater. Sol. Cells* **174**, 370–379 (2018).
- ²¹D. Davelou, G. Kopidakis, G. Kioseoglou, and I. N. Remediakis, "MoS₂ nanostructures: Semiconductors with metallic edges," *Solid State Commun.* **192**, 42–46 (2014).
- ²²A. Laturia, M. L. Van de Put, and W. G. Vandenberghe, "Dielectric properties of hexagonal boron nitride and transition metal dichalcogenides: from monolayer to bulk," *NPJ 2D Mater. Appl.* **2**, 1–7 (2018).
- ²³J. Gusakova, X. Wang, L. L. Shiao, A. Krivosheeva, V. Shaposhnikov, V. Borisenko, V. Gusakov, and B. K. Tay, "Electronic properties of bulk and monolayer TMDs: theoretical study within DFT framework (GVJ-2e method)," *phys. stat. sol.* **214**, 1700218 (2017).
- ²⁴M. Bokdam, G. Brocks, M. I. Katsnelson, and P. J. Kelly, "Schottky barriers at hexagonal boron nitride/metal interfaces: A first-principles study," *Phys. Rev. B* **90**, 085415 (2014).
- ²⁵J. Xiao, Y. Zhang, H. Chen, N. Xu, and S. Deng, "Enhanced performance of a monolayer MoS₂/WSe₂ heterojunction as a photoelectrochemical cathode," *Nanomicro Lett.* **10**, 1–9 (2018).
- ²⁶Z. Zhang, Y. Xie, Y. Ouyang, and Y. Chen, "A systematic investigation of thermal conductivities of transition metal dichalcogenides," *Int. j. heat mass transf.* **108**, 417–422 (2017).

- ²⁷X. Gu, B. Li, and R. Yang, "Layer thickness-dependent phonon properties and thermal conductivity of MoS₂," *J. Appl. Phys.* **119**, 085106 (2016).
- ²⁸Q. Cai, D. Scullion, W. Gan, A. Falin, S. Zhang, K. Watanabe, T. Taniguchi, Y. Chen, E. J. Santos, and L. H. Li, "High thermal conductivity of high-quality monolayer boron nitride and its thermal expansion," *Sci. Adv.* **5**, eaav0129, 1–8 (2019).
- ²⁹D. Wickramaratne, F. Zahid, and R. K. Lake, "Electronic and thermoelectric properties of few-layer transition metal dichalcogenides," *Chem. Phys.* **140**, 124710 (2014).
- ³⁰V. Mishra, S. Smith, L. Liu, F. Zahid, Y. Zhu, H. Guo, and S. Salahuddin, "Screening in ultrashort (5 nm) channel MoS₂ transistors: A full-band quantum transport study," *IEEE T-ED* **62**, 2457–2463 (2015).
- ³¹Y. Malozovsky, C. Bamba, A. Stewart, L. Franklin, and D. Bagayoko, "Accurate, ground state electronic and transport properties of h-bn," *BAPS* **65** (2020).
- ³²T. H. Ho, H. C. Dong, Y. Kawazoe, and H. M. Le, "Effect of elasticity of the MoS₂ surface on Li atom bouncing and migration: Mechanism from Ab initio molecular dynamic investigations," *J. Phys. Chem. C* **121**, 1329–1338 (2017).
- ³³M. M. Rehman, H. M. M. U. Rehman, J. Z. Gul, W. Y. Kim, K. S. Karimov, and N. Ahmed, "Decade of 2D-materials-based RRAM devices: a review," *STAM* **21**, 147–186 (2020).
- ³⁴H. Ghasemi, J. E. Rutledge, and H. Yazdani, "Mechanical properties of defective cyanoethynyl (2D polyaniline–C₃N): A comparative molecular dynamics study versus graphene and hexagonal boron nitride," *Physica E Low Dimens. Syst. Nanostruct.* **121**, 114085 (2020).
- ³⁵P. Zhuang, W. Lin, J. Ahn, M. Catalano, H. Chou, A. Roy, M. Quevedo-Lopez, L. Colombo, W. Cai, and S. K. Banerjee, "Nonpolar resistive switching of multilayer-hBN-based memories," *Adv. Electron. Mater.* **6**, 1900979 (2020).
- ³⁶D. J. J. Loy, P. A. Dananjaya, S. Chakrabarti, K. H. Tan, S. C. Chow, E. H. Toh, and W. S. Lew, "Oxygen vacancy density dependence with a hopping conduction mechanism in multilevel switching behavior of HfO₂-based resistive random access memory devices," *ACS Appl. Electron. Mater.* **2**, 3160–3170 (2020).
- ³⁷W. M. Haynes, D. R. Lide, and T. J. Bruno, *CRC handbook of chemistry and physics* (CRC press, 2016).
- ³⁸M. Eagleson *et al.*, *Concise encyclopedia chemistry* (Walter de Gruyter, 1994).
- ³⁹H.-C. Kim, H. Kim, J.-U. Lee, H.-B. Lee, D.-H. Choi, J.-H. Lee, W. H. Lee, S. H. Jhang, B. H. Park, H. Cheong, *et al.*, "Engineering optical and electronic properties of WS₂ by varying the number of layers," *ACS nano* **9**, 6854–6860 (2015).
- ⁴⁰X.-B. Li, N.-K. Chen, X.-P. Wang, and H.-B. Sun, "Phase-change superlattice materials toward low power consumption and high density data storage: Microscopic picture, working principles, and optimization," *Adv. Funct. Mater.* **28**, 1803380 (2018).